Journal of Membrane Science 752 (2026) 125622

Contents lists available at ScienceDirect

Journal of Membrane Science

journal homepage: www.elsevier.com/locate/memsci

In situ fabrication of sub-10 nm-thick *c*-oriented 2D Zn-TCPP membrane towards unprecedented CO_2/N_2 separation

Qidan Zheng [1], Sixing Chen [1], Meng Ge [*], Yi Liu, Taotao Ji, Chen Wang, Yifan Song, Yi Liu [**]

State Key Laboratory of Fine Chemicals, Frontiers Science Center for Smart Materials, School of Chemical Engineering, Dalian University of Technology, Dalian, 116024, China

ARTICLE INFO

Keywords:
Gas separation
Metal-organic frameworks
2D membranes
Nanosheets
Orientation

ABSTRACT

Realizing precise size-based sieving of CO_2/N_2 gas pairs represents a grand challenge due to their subtle difference in kinetic diameters. Aiming at high-efficiency carbon capture from flue gas, through facile in situ room-temperature growth, we prepared highly *c*-oriented sub-10 nm-thick two-dimensional (2D) Zn-TCPP (TCPP = tetrakis(4-carboxyphenyl)porphyrin) membrane with 0.36 nm sieving channels under ambient conditions perpendicular to the substrate surface, relying on regular AB stacking between adjacent single layers with 1/2 uniform dislocation in both *a* and *b* directions. Owing to the well-defined interlayer structure of 2D Zn-TCPP nanosheets which matches closely with the kinetic diameter of CO_2 molecules (3.3 Å) and effectively hinders the transport of larger N_2 molecules (3.64 Å), together with strong quadrupole-dipole interactions between CO_2 and 2D Zn-TCPP framework, the obtained membrane exhibited unprecedented CO_2/N_2 selectivity up to ~120, which transcended state-of-the-art MOF membranes reported in the literature. The above unique structural precision and preferential CO_2 adsorption rendered 2D Zn-TCPP membrane highly promising for practical carbon capture from flue gas.

1. Introduction

High-efficiency carbon capture from flue gas (i.e., CO_2/N_2 separation) is significant for realizing carbon capture, utilization and storage (CCUS) [1]. Among various potential technologies, membrane-based separation has shown bright prospect because of its inherent advantages in terms of high energy efficiency, compact footprint, low cost, and operational simplicity [2–8]. Recently, two-dimensional (2D) membrane materials, such as graphene oxide (GO), 2D metal-organic framework (MOF), and 2D covalent-organic framework (COF), have attracted significant attention due to their atomic-scale thickness, minimal mass transfer resistance and diverse diffusion pathways [9]. These features offer great potential to overcome the long-standing permeability-selectivity trade-off [10–13]. Among them, 2D MOF membranes offer unique advantages in terms of uniform and well-defined pore aperture, rich functional groups, and easy processing, rendering them highly promising for high-efficiency CO_2/N_2 separation [14–16]. However, translating these advantages into practice remains quite challenging. On the one hand, it is difficult to precisely tailor the in-plane pore size, geometry, and uniformity while simultaneously regulating the interlayer channel architecture of the membrane at the microscopic scale [17–19]; on the other hand, accurate control of crystal orientation, grain boundary defect density, and membrane continuity at the mesoscopic scale still relies heavily on trial-and-error [20–24].

In recent decades, preferred orientation has been proven to exert significant influence on gas separation performance of MOF membranes. In terms of CO_2/N_2 separation, we fabricated highly (111)-oriented UiO-66 membrane with a thickness of 165 nm through oriented epitaxial growth. The obtained membrane exhibited CO_2 permeance of 2070 gas permeation units (GPU) and CO_2/N_2 selectivity of 35.4 under ambient conditions [25]. To further enhance CO_2 affinity, we fabricated highly *c*-oriented NH_2-MIL-125 membrane functionalized with Cu(I) ions, where π-complexation interactions afforded improved CO_2/N_2 selectivity of 43.2 [26]. Very recently, by introducing missing-linker defects

* Corresponding author.
** Corresponding author.
E-mail addresses: gemeng@dlut.edu.cn (M. Ge), diligenliu@dlut.edu.cn (Y. Liu).
[1] Co-first author: Qidan Zheng and Sixing Chen contributed equally to this work.

https://doi.org/10.1016/j.memsci.2026.125622
Received 13 March 2026; Received in revised form 21 April 2026; Accepted 3 May 2026
Available online 4 May 2026

into the MIL-125 framework, an exceptional CO_2/N_2 selectivity as high as 47.7 was achieved, demonstrating the great potential of multi-scale structure optimization in achieving superior CO_2/N_2 separation [27]. However, the enhanced CO_2/N_2 selectivity of MOF membranes mainly originates from preferential CO_2 adsorption. In contrast, size-sieving-based separation, which relies on molecular discrimination based on slight differences in kinetic diameters, remains highly challenging due to the difficulty in precisely controlling pore sizes within the range of 3.4-3.6 Å. In terms of CO_2 permeance, membrane thickness and preferred orientation cooperatively play a decisive role. Ideally, vertically aligned straight channels combined with an ultrathin selective layer (<10 nm) enable minimized transport resistance [28,29]. Nonetheless, it remains quite challenging to concurrently achieve a high degree of preferred orientation and ultrathin thickness due to the lack of viable synthetic protocols that enable accurate crystal orientation control while simultaneously suppressing excessive layer thickening during membrane processing.

Tetrakis(4-carboxyphenyl)porphyrin (TCPP)-derived 2D MOF provides a unique platform for exerting precise control over pore size since the pore aperture can be finely tuned via facile stacking mode engineering [30]. Specifically, 2D Zn-TCPP, which is formed through ordered coordination between TCPP ligands and Zn^{2+} ions, generating a single layer with large in-plane pores of 11.8 Å, adopts a distinctive 1/2 AB dislocation stacking between adjacent single layers [31]. This unique stacking mode substantially alters the through-plane pore geometry. The equivalent pore aperture along the *c*-axis is determined to be ~3.6 Å based on physical adsorption measurements, which just falls between the kinetic diameters of CO_2 and N_2 (Fig. 1a), enabling the realization of precise size-sieving-based separation. In addition, considering the importance of membrane thickness and preferred orientation control, fabrication of highly *c*-oriented ultrathin 2D Zn-TCPP membrane is preferred. It is therefore expected that integrating 2D TCPP-derived stacking precision with oriented ultrathin microstructure represents a compelling strategy for pushing CO_2/N_2 separation performance beyond current limits.

In this study, we pioneered the room temperature (RT) synthesis of highly *c*-oriented sub-10 nm-thick 2D Zn-TCPP membrane through facile in situ synthesis (Fig. 1b). RT synthesis features mild reaction conditions, low energy consumption, and excellent scalability, rendering it a promising strategy for industrial membrane manufacturing [32]. The 1/2 AB dislocation stacking between adjacent layers reduced the *c*-axis channel size to 3.6 Å under ambient conditions, which fell between the kinetic diameters of CO_2 and N_2, enabling efficient size-sieving transport, despite minor framework fluctuations. This well-defined structural precision, accompanied by preferential CO_2 adsorption, endowed our membrane with unprecedented CO_2/N_2 selectivity up to ~120, which ranked the highest among state-of-the-art MOF membranes measured under ambient conditions, demonstrating great promise for high-efficiency carbon capture from flue gas.

2. Methods

2.1. Preparation of 2D Zn-TCPP NSs

TCPP (2 mg) was added into 12 mL of N-methylformamide (NMF) and stirred at RT for 30 min. Subsequently, 2 mL of $Zn(NO_3)_2{\cdot}6H_2O$ aqueous solution (2.5 mg/mL) was added to the TCPP solution. After stirring for 5 min at RT, the obtained solid products were centrifuged and sequentially washed three times with ethanol (EtOH). Finally, the solid products were dried overnight at 70 °C.

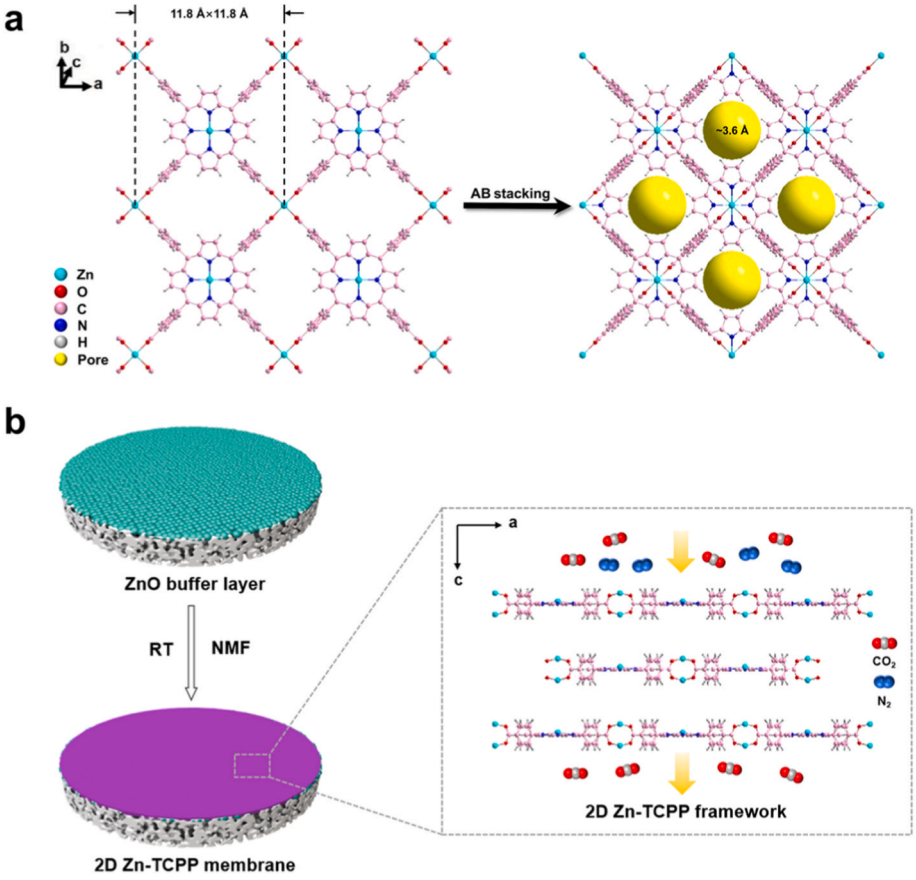

Fig. 1. (a) Schematic diagram of narrowed pore size of Zn-TCPP membrane in comparison with a single Zn-TCPP layer (Zn: light blue, C: pink, N: blue, O: red, H: grey, and pore: yellow). (b) Schematic illustration of the preparation of highly *c*-oriented ultrathin 2D Zn-TCPP membrane. (For interpretation of the references to colour in this figure legend, the reader is referred to the Web version of this article.)

2.2. Preparation of gel-based ZnO buffer layer

Initially, the ZnO sol was obtained by adding 8.3 g Zn $(CH_3COO)_2{\cdot}2H_2O$ to 48 mL EtOH solution at 70 °C under vigorous stirring. Subsequently, 2.25 mL ethanolamine was added dropwise at a rate of 0.6 mL/min to the solution at 70 °C under stirring at 500 rpm for 30 min. In the next step, the solution was aged at 25 °C for 24 h. Finally, the ZnO buffer layer was obtained by spin-coating at 3000 rpm for 60 s, followed by calcination at 400 °C for 2 h with a heating rate of 1 °C/min.

2.3. Preparation of 2D Zn-TCPP membrane

Initially, 2 mg TCPP ligands were added to 12 mL NMF and stirred at RT for 30 min. Subsequently, the ZnO buffer layer-modified substrate was vertically placed into the solution. In the next step, the Teflon-lined vessel was put in an oven at 25 °C for 6 h. Finally, the obtained 2D Zn-TCPP membrane was washed with EtOH and dried overnight at RT.

3. Results and discussion

3.1. Preparation of 2D Zn-TCPP nanosheets (NSs)

Ultrathin 2D MOF NSs were traditionally obtained via a top-down approach, such as ultrasonication-induced delamination of bulk crystals, in which adjacent single layers were assembled together by weak van der Waals forces [30]. Alternatively, bottom-up synthesis offers obvious advantages in terms of better control over NS morphology and structural integrity [33–35]. It should be noted that above methods typically involve the modulation of nucleation and growth kinetics through optimizing solvent composition, ligand deprotonation rate, metal-to-ligand ratio, and reaction temperature. Our recent investigation revealed that solvent type could serve as a powerful tool for regulating ligand deprotonation rate of H_2TCPP. In this study, we pioneered mild synthesis of uniform ultrathin 2D Zn-TCPP NSs through solvent optimization. Our results indicated that the use of NMF solvent not only enabled the formation of NSs with optimized structure but also warranted significant reduction in reaction temperature from 150 °C to RT (Fig. S1).

Initially, we explored the use of different solvents with varying deprotonation abilities, e.g., DMF, formamide and NMF, for the preparation of 2D Zn-TCPP NSs. Experimental results indicated that with DMF as the solvent, 2D Zn-TCPP crystals with block-like morphology could be obtained (Fig. S1a), while using formamide as solvent resulted in the formation of 2D Zn-TCPP crystals with rod-like morphology (Fig. S1b). In contrast, employing NMF as solvent resulted in the generation of 2D Zn-TCPP crystals with unique sheet-like morphology (Fig. S1c). Therefore, NMF was identified as the optimal solvent for synthesizing 2D Zn-TCPP NSs. To further optimize their morphology, we tried dropwise addition of the metal solution into ligand solution, followed by vigorous stirring during the whole period, ultimately leading to the formation of uniform 2D Zn-TCPP NSs with a thickness of 7 nm (Fig. 2a–d). Obtained NSs were investigated by HRTEM with the electron beam oriented along the *c*-axis, providing a direct projection of the *a*-*b* plane of the framework (Fig. 2e). The corresponding structural model superimposed in

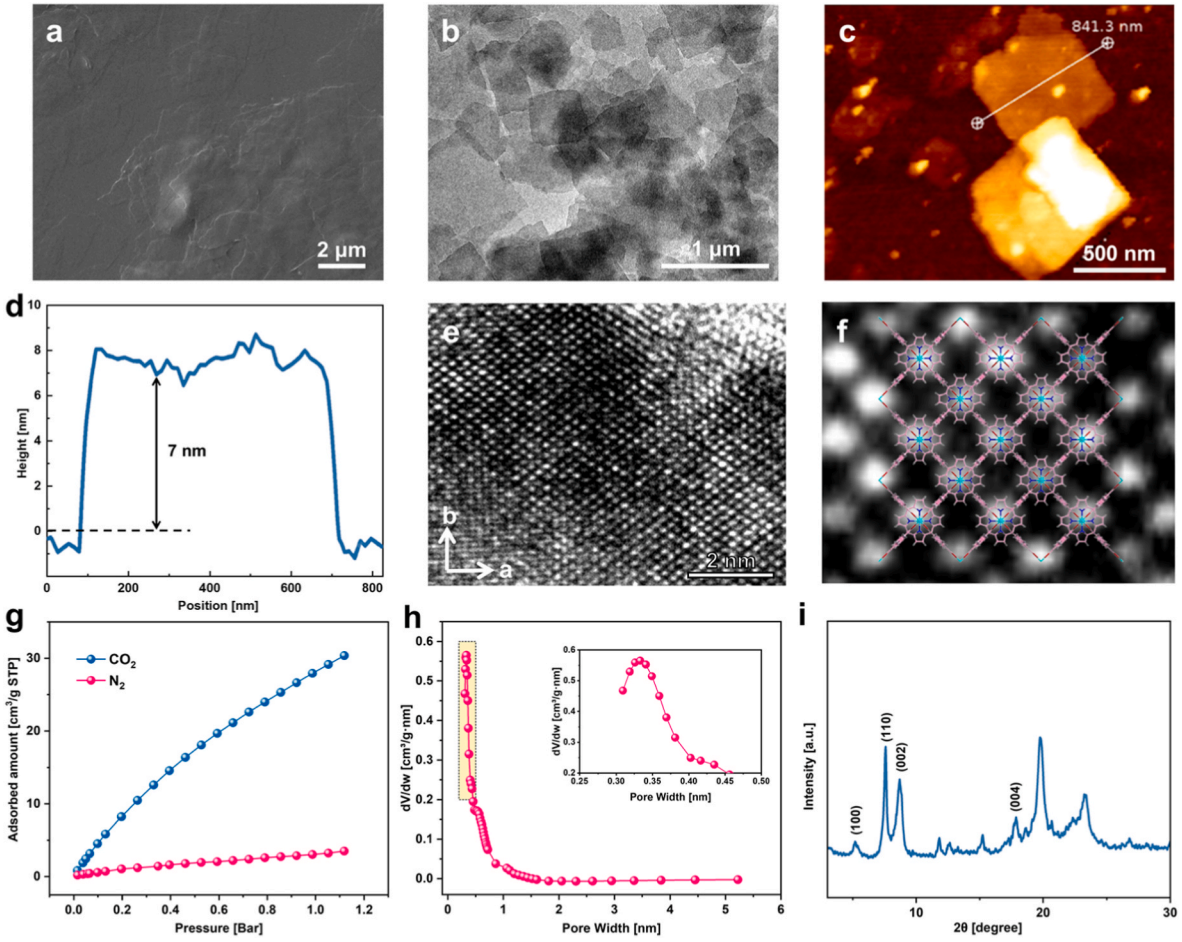

Fig. 2. (a) SEM image, (b) TEM image, (c) AFM image and (d) AFM height profile of 2D Zn-TCPP NSs. (e, f) HRTEM image of 2D Zn-TCPP NSs viewed along the *c*-axis. (g) CO_2 and N_2 adsorption isotherms (298 K), (h) pore size distribution derived from the H–K model (inset: N_2 adsorption isotherm at 77 K) and (i) XRD pattern of 2D Zn-TCPP NSs.

Fig. 2f further confirmed that the observed lattice features matched the expected 2D Zn-TCPP framework viewed along the *c*-axis.

Textural properties of obtained 2D Zn-TCPP NSs were further investigated. CO_2 and N_2 physical adsorption results showed preferential adsorption of CO_2 over N_2 with CO_2/N_2 IAST selectivity of 18.2 (Fig. 2g and S2). Benefiting from the precisely tailored 3.6 Å interlayer aperture and strong electrostatic interactions between CO_2 and polar sites in the porphyrin-Zn^{2+} framework, the 2D Zn-TCPP NSs showed preferential CO_2 adsorption over N_2, enabling highly selective CO_2 transport. In addition, the pore size distribution of the obtained 2D Zn-TCPP NSs (Fig. 2h) was calculated using the Horváth-Kawazoe (H–K) model, yielding a pore size centered at 0.36 nm. This value is fully consistent with the theoretical pore aperture (3.6 Å) generated by the 1/2 AB dislocation-type stacking in 2D Zn-TCPP with detailed calculation procedure provided in Fig. S3. Such stacking-induced constriction effectively tailored the transport channels to the dimension well suited for precise CO_2/N_2 screening. In addition, XRD patterns of obtained NSs exhibited well-defined reflections at 8.7° and 17.8° (Fig. 2i), which could be indexed to (002) and (004) planes of 2D Zn-TCPP NSs, respectively. The sharpness and high intensity of above peaks confirmed their high crystallinity, ordered stacking, and preferential *c*-orientation. TG analysis further revealed that obtained 2D Zn-TCPP NSs possessed exceptional thermal stability with decomposition onset temperature of 400 °C (Fig. S4), ensuring that their structural integrity and framework precision could be well maintained under practical operation conditions.

Subsequently, we attempted to deposit 2D Zn-TCPP NSs onto a porous α-Al_2O_3 substrate through thermal drop-coating. Previous studies reported that vacuum hot drop-coating could assemble high-aspect-ratio 2D NSs into continuous layers through accelerating solvent removal, suppressing coffee-ring flows, and improving NS-substrate adhesion for face-on alignment [21,36]. In this study, however, the resulting layer did not exhibit the desired morphology. As shown in Fig. S5a, relevant SEM image revealed that 2D Zn-TCPP NSs were unevenly distributed on the substrate surface with each NS in close contact with its neighbors, inevitably leading to the generation of grain boundary defects in the layer. To be specific, localized wrinkles and curled edges were clearly visible, which were characteristic of intrinsic flexibility of ultrathin 2D NSs, adversely affecting gas sieving properties of the obtained layer. It should be noted that although a uniform and continuous layer with thickness of 170 nm could be obtained under optimized conditions (Fig. S5b and c), its ideal CO_2/N_2 selectivity was close to the Knudsen selectivity, which was indicative of the existence of substantial grain boundary defects in the membrane. Although conducting epitaxial growth may patch above non-selective defects, both its thickness and preferred orientation may be compromised, thus negatively affecting the CO_2/N_2 separation performance [37,38].

Aiming at maintaining both process simplicity and structure superiority, alternatively, in situ growth was adopted to prepare 2D Zn-TCPP membrane on porous α-Al_2O_3 substrate. It is expected that heterogeneous nucleation can dominantly occur on the substrate surface rather than in the bulk solution so that excessive bulk crystallization can be suppressed [39–41], enabling the formation of 2D Zn-TCPP membrane with desired microstructure.

3.2. Preparation of c-oriented ultrathin 2D Zn-TCPP membranes

Subsequently, we chose to in situ grow 2D Zn-TCPP membrane directly on porous α-Al_2O_3 substrate (Fig. S6). Nonetheless, our results revealed that it was impossible to obtain a continuous membrane through simple reaction condition optimization (Fig. S7a), owing to the low nucleation density at the solution-substrate interface. Moreover, using γ-Al_2O_3 and ZrO_2 as alternative buffer layers still yielded membranes with inferior continuity and orientation (Fig. S7b and S7c). To address this issue, a uniform ZnO buffer layer was fabricated on the substrate via a sol-gel method followed by calcination prior to in situ growth (Fig. 3a). With this buffer layer, a continuous, highly *c*-oriented ultrathin 2D Zn-TCPP membrane was successfully obtained (Fig. 3b and c). Based on control experiments and characterization, the key roles of the ZnO buffer layer can be summarized as follows. First, it increases the interfacial nucleation density, which is beneficial for continuous membrane formation. Second, it promotes preferred orientation. The ZnO buffer layer also acts as an active layer that favors *c*-oriented growth of Zn-TCPP crystallites since taking this configuration warrants the largest crystal face to contact the substrate surface, which is favorable for maximizing face-to-face interfacial contact and lowering overall interfacial energy [42]. Third, it strengthens membrane-substrate adhesion through partial infiltration into the substrate pores, which is supported by relevant EDXS results (Fig. S8). Accordingly, the promoting effect of the ZnO buffer layer originates from combined interfacial chemical and structural contributions. As expected, XRD results (Fig. 3d) confirmed that the obtained buffer layer was pure wurtzite ZnO with a smooth morphology.

ATR-IR and XPS spectra were further employed to study textural properties of obtained 2D Zn-TCPP membrane. It was observed that there existed $Zn_2(COO)_4$ paddle-wheel unit in the framework, which was consistent with Zn-based secondary building units of 2D Zn-TCPP phase as reported in the literature. As shown in Fig. 3e, ATR-IR spectra of both Zn-TCPP powders and membrane showed absorption peaks around 1600 cm^{-1} and 1400 cm^{-1}, which could be assigned to the C═O asymmetric stretching vibration (ν_{asym}C═O) and the C═O symmetric stretching vibration (ν_{sym}C═O), respectively. These results confirmed the formation of coordination bonds between carboxyl groups of H_2TCPP ligands and Zn-based secondary building units; moreover, as shown in XPS spectra (Fig. 3f–i), C 1s peaks at 284 eV and 288 eV corresponded to C–C and C═O bonds in 2D Zn-TCPP framework, while Zn 2p spectra showed two characteristic peaks at 1022 eV and 1045 eV, which could be assigned to the Zn $2p_{1/2}$ and Zn $2p_{3/2}$ spin-orbit states, respectively. The above results were consistent with the peak position in XPS spectra of 2D Zn-TCPP in the literature, further confirming the formation of 2D Zn-TCPP membrane [43]. It should be noted that relevant XPS spectra showed a weak Al element peak (Fig. 3i), implying that the average thickness of the 2D Zn-TCPP membrane should be below the XPS detection upper limit of 10 nm.

The thickness of the 2D Zn-TCPP membrane supported on the substrate was directly measured from FIB-prepared cross-sectional TEM images as ~9 nm (Fig. 4a). Owing to the high electron transparency of the ultrathin lamella, the cross-section permitted direct atomic-scale imaging of 2D Zn-TCPP framework within an intact MOF thin film. This represented, to the best of our knowledge, the first instance in which the lattice of porphyrinic-based MOF membranes was directly resolved in cross-sectional view. The enlarged HRTEM image (Fig. 4b) clearly resolved the periodic lattice of the framework, confirming the high crystallinity and structural coherence of the membrane in the observed region. Further HRTEM analysis (Fig. 4c) revealed the characteristic 1/2 AB dislocation-type stacking between adjacent 2D Zn-TCPP single layers. Consistently observed in all investigated regions, these features confirmed the preferred *c*-orientation and ordered interlayer registry (Fig. S9), supported by the prominent (004) diffraction peak in XRD and homogeneous, continuous morphology in large-scale SEM observations. This ordered half-shifted packing has not previously been reported for any TCPP-based MOF films/membranes and therefore provides direct structural insights into the intrinsic layer registry of this material. The two pink guidelines in Fig. 4c indicated the *c*-axis direction, along which equivalent one-dimensional pore aperture was measured to be 3.6 Å. This value lay between the kinetic diameters of CO_2 (3.30 Å) and N_2 (3.64 Å), offering the first direct microscopic evidence that porphyrinic-based MOF membranes enabled angstrom-level molecular sieving. The corresponding structural model superimposed in Fig. 4d further confirmed that the observed lattice features matched the expected 2D Zn-TCPP framework viewed along the *b*-axis. The HRTEM image, acquired along the *b*-axis and thus showing the

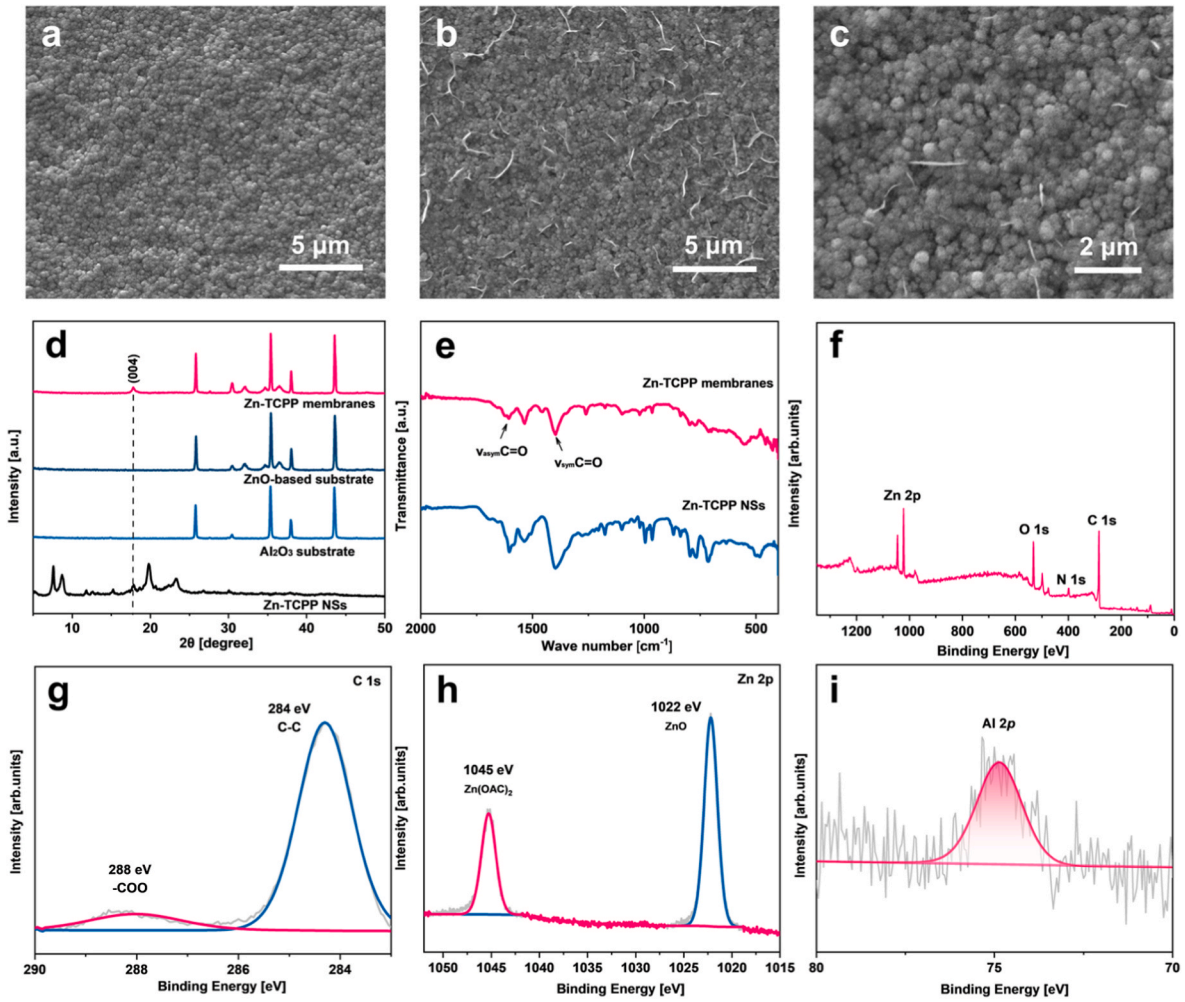

Fig. 3. SEM images of (a) ZnO buffer layer-coated porous α-Al_2O_3 substrate and (b, c) 2D Zn-TCPP membrane. (d) XRD patterns of porous α-Al_2O_3 substrate, ZnO buffer layer-coated porous α-Al_2O_3 substrate, and 2D Zn-TCPP membranes. (e) ATR-IR spectra of 2D Zn-TCPP NSs and membrane. (f-i) XPS spectra of 2D Zn-TCPP membrane.

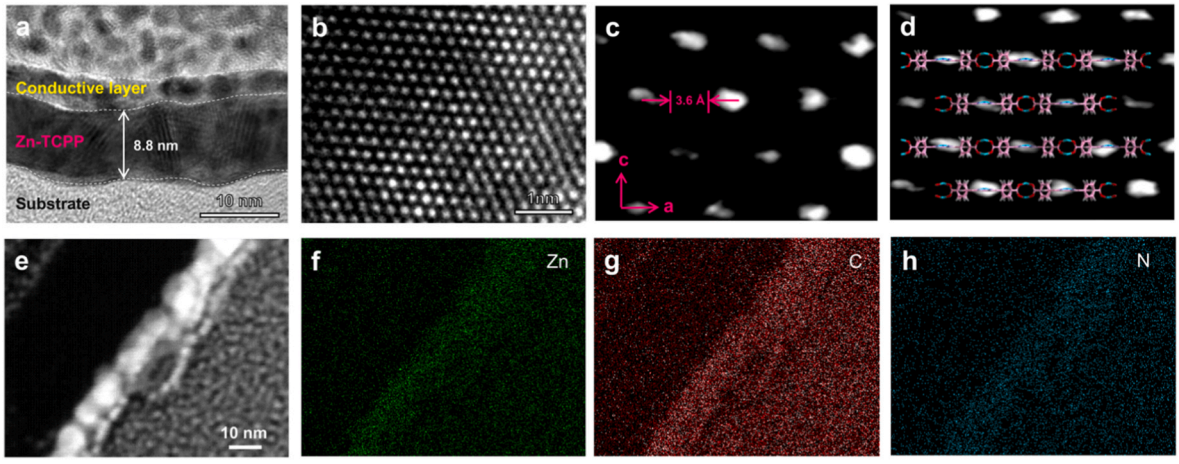

Fig. 4. (a-c) HRTEM images of the cross-section of 2D Zn-TCPP membrane. (d) HRTEM image of 2D Zn-TCPP framework with a superimposed structural model. (e) STEM image of the cross-section of 2D Zn-TCPP membrane with elemental distribution maps of (f) Zn, (g) C, and (h) N.

atomic arrangement in the *a-c* plane, revealed a distinctly stratified morphology in which the 2D Zn-TCPP layers were composed of well-resolved atomic-column dots arranged in a periodic lattice; simultaneously, adjacent layers exhibited a characteristic half-shifted alignment. Fig. 4d highlighted the clear atomic columns and the orderly 1/2-shifted stacking between neighboring layers. These periodically spaced sheet-like features were fully consistent with the intrinsic layered architecture of 2D Zn-TCPP, where porphyrin linkers coordinated with

Zn-oxo nodes to form extended 2D slabs that stacked along the *b*-axis direction. Fig. 4e showed the cross-sectional STEM image of the 2D Zn-TCPP membrane. The accompanying elemental maps of Zn, C, and N (Fig. 4f–h) exhibited uniform and co-localized distributions throughout the membrane region, confirming homogeneous composition of 2D Zn-TCPP framework and uniform microstructure of the membrane.

It should be noted that in order to obtain the 2D Zn-TCPP membrane with desired microstructure, the reaction duration has to be accurately controlled at 6 h. Further prolonging the reaction duration to 12 h inevitably led to secondary nucleation in the bulk solution and therefore, sedimentation of bulk 2D Zn-TCPP nuclei on the substrate, followed by undesired twin formation through van der Drift selection mechanism (Fig. S10a–c). As shown in Fig. S10c, we observed that 2D Zn-TCPP crystallites were vertically aligned on the substrate surface, while XRD results confirmed that the diffraction intensity of (100) and (110) peaks appeared accompanying with the increase of (004) peak, demonstrating that the dominance of preferred *c*-orientation could no longer be preserved (Fig. S10d).

3.3. Gas separation performance of 2D Zn-TCPP membranes

Aiming at evaluating its CO_2/N_2 separation performance, gas permeation behavior of obtained 2D Zn-TCPP membrane was measured. Relevant single gas permeation results revealed that our membrane exhibited the highest average CO_2 permeance compared with H_2, N_2 and CH_4, attributing to preferential CO_2 adsorption (Table 1). Correspondingly, average ideal selectivity (IS) for CO_2/N_2, CO_2/H_2 and CO_2/CH_4 gas pairs attained 123.5, 25.9 and 17.0, respectively. Compared with other molecular sieve membranes reported in the literature, our membrane exhibited the highest CO_2/N_2 selectivity under comparable conditions, thus transcending the limits of state-of-the-art molecular sieve membranes for CO_2/N_2 separation (Fig. 5). Even when tested with an equimolar CO_2/N_2 gas pair under ambient conditions, our membrane still exhibited CO_2/N_2 separation factor (SF) of 115.4 (Table 1), confirming its ability to accurately screen CO_2 from N_2, which was indispensable for practical carbon capture from flue gas. In mixed-gas measurements, the CO_2 permeance reached 237.9 GPU, which was mainly attributed to the combined mass transfer resistance from the porous substrate, ZnO interlayer, subnanometer channels, and partial interfacial pore blockage. The ZnO interlayer contributed significantly to diffusion resistance by infiltrating substrate pores and reducing gas transport pathways, while the narrow subnanometer channels within the membrane also introduced intrinsic resistance despite enabling high CO_2/N_2 selectivity. The outstanding CO_2/N_2 separation performance indicated the presence of well-defined, size-selective sieving channels at room temperature. Based on the IAST CO_2/N_2 adsorption selectivity of 18.2, the diffusion selectivity was estimated to be approximately 6.8, highlighting the synergistic contribution of preferential adsorption and size sieving to the overall separation performance.

4. Conclusions

In this study, we pioneered the room-temperature synthesis of uniform ultrathin 2D Zn-TCPP NSs. Among various factors, using NMF as solvent was found to play a crucial role in obtaining desired microstructure of the material. Through facile in situ growth, highly *c*-oriented sub-10 nm-thick 2D Zn-TCPP membrane could be readily obtained under mild reaction conditions. HRTEM analysis convincingly demonstrated the atomically precise 1/2 AB dislocation-type stacking between adjacent single layers, forming vertically aligned 0.36 nm sieving channels under ambient conditions, which fell between the kinetic diameters of CO_2 and N_2 molecules. Owing to the precisely tailored interlayer architecture as well as strong quadrupole-dipole interaction between CO_2 and 2D Zn-TCPP framework, our membrane exhibited CO_2/N_2 selectivity as high as 123.5, which ranked the highest among state-of-the-art molecular sieve membranes, showing great promise for practical carbon capture from flue gas. Moreover, the room-temperature synthesis offers an energy-efficient and safer alternative to conventional approaches, facilitating scalable fabrication in future practical applications.

Table 1
Gas separation performance of 2D Zn-TCPP membrane.

Gas pair	Single gas		Mixed gas	
	CO_2 Permeance (GPU)	IS	CO_2 Permeance (GPU)	SF
CO_2/H_2	191.1	25.9	186.5	11.1
CO_2/N_2		123.5	237.9	115.4
CO_2/CH_4		17.0	175.4	12.1

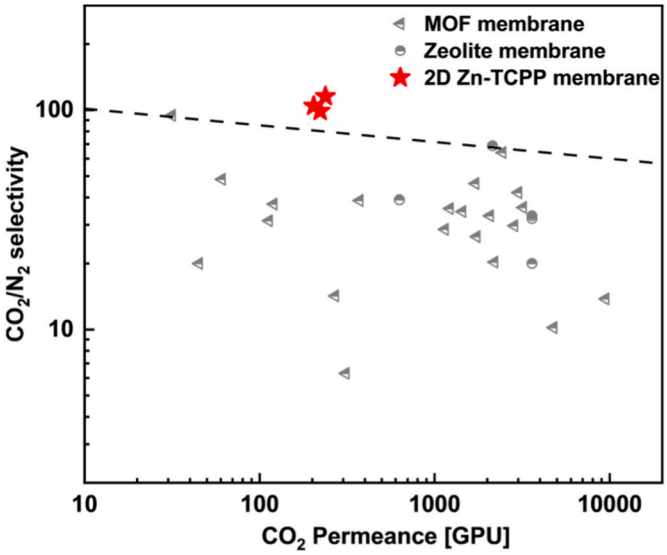

Fig. 5. Comparison of the CO_2/N_2 separation performance of 2D Zn-TCPP membrane with other molecular sieve membranes reported in the literature (detailed data are listed in Table S1).

CRediT authorship contribution statement

Qidan Zheng: Data curation, Investigation, Writing – original draft. **Sixing Chen:** Data curation, Investigation, Methodology, Writing – original draft. **Meng Ge:** Data curation, Supervision, Writing – review & editing. **Yi Liu:** Formal analysis, Data curation. **Taotao Ji:** Formal analysis, Investigation. **Chen Wang:** Investigation. **Yifan Song:** Formal analysis, Methodology. **Yi Liu:** Conceptualization, Funding acquisition, Methodology, Resources, Supervision, Writing – review & editing.

Declaration of competing interest

The authors declare that they have no known competing financial interests or personal relationships that could have appeared to influence the work reported in this paper.

Acknowledgements

The authors are grateful to the National Natural Science Foundation of China (22478056, 22408038), China Postdoctoral Science Foundation (2025M771168), Liaoning Province Funds for Distinguished Young Scholars (2024JH3/50100002), National Key Research and Development Program of China (2023YFB3810700), State Key Laboratory of Catalysis (2024SKL-A-003), and Science and Technology Innovation Fund of Dalian (2024JJ12GX027) for the financial support.

Appendix A. Supplementary data

Supplementary data to this article can be found online at https://doi.org/10.1016/j.memsci.2026.125622.

Data availability

The authors do not have permission to share data.

References

[1] X. Wang, C. Song, Carbon capture from flue gas and the atmosphere: a perspective, Front. Energy Res. 8 (2020) 560849.
[2] A.I. Osman, Z. Chen, A.M. Elgarahy, M. Farghali, I.M.A. Mohamed, A.K. Priya, H. B. Hawash, P. Yap, Membrane technology for energy saving: principles, techniques, applications, challenges, and prospects, Adv. Energy Sustain. Res. 5 (2024) 2400011.
[3] Z. Song, Y. Wang, Z. Zha, Z. Wang, S. Zhao, Porous organic cage separation membranes: exploratory journey from preparation to application, Adv. Membr. 5 (2025) 100125.
[4] S. Zhou, Y. Wei, L. Li, Y. Duan, Q. Hou, L. Zhang, L.-X. Ding, J. Xue, H. Wang, J. Caro, Paralyzed membrane: current-driven synthesis of a metal-organic framework with sharpened propene/propane separation, Sci. Adv. 4 (2018) eaau1393.
[5] D. Li, M. Ye, C. Ma, N. Li, Z. Gu, Z. Qiao, Preparation of a self-supported zeolite glass composite membrane for CO_2/CH_4 separation, Smart Mol. 2 (2024) e20240009.
[6] Y. Wang, B. Yan, J. Liu, R. Wang, P. Rao, Y. Liu, Advances in MOF membrane strategies for selective lithium extraction from salt lake brine, Adv. Membr. 5 (2025) 100156.
[7] J.M. Restrepo-Flórez, M. Maldovan, Breaking separation limits in membrane technology, J. Membr. Sci. 566 (2018) 301–306.
[8] X. Li, J. Yu, S. Han, Y. Zhou, Y. Liang, Y. Wang, Z. Wang, Ligand substitution engineering for modulating the pore microenvironment of MOFs to enhance CO_2 gas separation performance in mixed matrix membranes, Adv. Membr. 7 (2026) 100210.
[9] C. Ji, H. Shao, Y. Pu, H. Zhang, H. Li, W. Li, N. Zhu, W. Zhao, D. Jiang, D. Zhao, 2D open framework materials: chemistry, materials, and applications, Adv. Mater. 37 (2025) e13499.
[10] D. Chen, W. Ying, Y. Guo, Y. Ying, X. Peng, Enhanced gas separation through nanoconfined ionic liquid in laminated MoS_2 membrane, ACS Appl. Mater. Interfaces 9 (2017) 44251–44257.
[11] H.W. Kim, H.W. Yoon, S.-M. Yoon, B.M. Yoo, B.K. Ahn, Y.H. Cho, H.J. Shin, H. Yang, U. Paik, S. Kwon, J.-Y. Choi, H.B. Park, Selective gas transport through few-layered graphene and graphene oxide membranes, Science 342 (2013) 91–95.
[12] K.V. Agrawal, X. Zhang, B. Elyassi, D.D. Brewer, M. Gettel, S. Kumar, J.A. Lee, S. Maheshwari, A. Mittal, C.Y. Sung, M. Cococcioni, L.F. Francis, A.V. McCormick, K.A. Mkhoyan, M. Tsapatsis, Dispersible exfoliated zeolite nanosheets and their application as a selective membrane, Science 334 (2011) 72–75.
[13] X. Liu, P. Liu, H. Wang, N.M. Khashab, Advanced microporous framework membranes for sustainable separation, Adv. Mater. 37 (2025) 2500310.
[14] J. Zhao, G. He, Y. Chen, S. Dong, Z. Jiang, W. Jin, Engineering high-flux 2D separation membranes: fundamentals, strategies, and future directions, Adv. Funct. Mater. 35 (2025) e11844.
[15] Y. Peng, Y. Li, Y. Ban, H. Jin, W. Jiao, X. Liu, W. Yang, Metal-organic framework nanosheets as building blocks for molecular sieving membranes, Science 346 (2014) 1356–1359.
[16] D. Lee, S. Lee, I. Choi, M. Kim, Positional functionalizations of metal-organic frameworks through invasive ligand exchange and additory MOF-on-MOF strategies: a review, Smart Mol. 2 (2024) e20240002.
[17] H. Fan, A. Mundstock, A. Feldhoff, A. Knebel, J. Gu, H. Meng, J. Caro, Covalent organic framework-covalent organic framework bilayer membranes for highly selective gas separation, J. Am. Chem. Soc. 140 (2018) 10094–10098.
[18] Y. Li, Q. Wu, X. Guo, M. Zhang, B. Chen, G. Wei, X. Li, X. Li, S. Li, L. Ma, Laminated self-standing covalent organic framework membrane with uniformly distributed subnanopores for ionic and molecular sieving, Nat. Commun. 11 (2020) 599.
[19] Z. Chen, Z. Xu, X. Zhong, Y. Chen, S. Yang, Y. Feng, P. Zhang, Y. Li, M. Xue, X. Chen, Coordination polymer glass-unified MOF membranes for high-efficiency molecular separations, Adv. Mater. 38 (2026) e12654.
[20] Y. Li, H. Liu, H. Wang, J. Qiu, X. Zhang, GO-guided direct growth of highly oriented metal-organic framework nanosheet membranes for H_2/CO_2 separation, Chem. Sci. 9 (2018) 4132–4141.
[21] X. Wang, C. Chi, K. Zhang, Y. Qian, K.M. Gupta, Z. Kang, J. Jiang, D. Zhao, Reversed thermo-switchable molecular sieving membranes composed of two-dimensional metal-organic nanosheets for gas separation, Nat. Commun. 8 (2017) 14460.
[22] T. Xia, Y. Wu, T. Ji, W. Hu, K. Yu, X. He, B.H. Yin, Y. Liu, Mixed-matrix membranes incorporating hierarchical ZIF-8 towards enhanced CO_2/N_2 separation, Smart Mol. 3 (2025) e20240066.
[23] Q. Hou, S. Zhou, Y. Wei, J. Caro, H. Wang, Balancing the grain boundary structure and the framework flexibility through bimetallic metal-organic framework (MOF) membranes for gas separation, J. Am. Chem. Soc. 142 (2020) 9582–9586.
[24] H. Wang, C. Zhang, L. Fan, Z. Kang, D. Sun, Combining zeolite with MOF glass to construct crystal-glass composite membranes for improved hydrogen separation, Adv. Membr. 5 (2025) 100164.
[25] Y. Sun, J. Yan, Y. Gao, T. Ji, S. Chen, C. Wang, P. Lu, Y. Li, Y. Liu, Fabrication of highly oriented ultrathin zirconium metal-organic framework membrane from nanosheets towards unprecedented gas separation, Angew. Chem. Int. Ed. 62 (2023) e202216697.
[26] Y. Sun, S. Hu, J. Yan, T. Ji, L. Liu, M. Wu, X. Guo, Y. Liu, Oriented ultrathin π-complexation MOF membrane for ethylene/ethane and flue gas separations, Angew. Chem. Int. Ed. 62 (2023) e202311336.
[27] C. Wang, J. Yan, S. Meng, Y. Wu, S. Chen, Y. Sun, X. Li, B. Sun, G. He, Y. Liu, Fabrication of highly C-oriented defect-rich MIL-125 membrane from nanosheets towards exceptional CO_2/N_2 separation, J. Membr. Sci. 711 (2024) 123185.
[28] G. Liu, W. Jin, N. Xu, Two-dimensional-material membranes: a new family of high-performance separation membranes, Angew. Chem. Int. Ed. 55 (2016) 13384–13397.
[29] P. Pandey, R.S. Chauhan, Membranes for gas separation, Prog. Polym. Sci. 26 (2001) 853–893.
[30] Y. Peng, Y. Li, Y. Ban, W. Yang, Two-dimensional metal-organic framework nanosheets for membrane-based gas separation, Angew. Chem. Int. Ed. 56 (2017) 9757–9761.
[31] X. Lei, S.W. Tay, P.J. Ong, L. Hong, Organic dye solution nanofiltration by 2D Zn-TCPP(Fe) membrane-leverage of chemical and fluid dynamic effects, J. Ind. Eng. Chem. 78 (2019) 410–420.
[32] J. Yan, Y. Sun, T. Ji, C. Zhang, L. Liu, Y. Liu, Room-temperature synthesis of defect-engineered Zirconium-MOF membrane enabling superior CO_2/N_2 selectivity with zirconium-oxo cluster source, J. Membr. Sci. 653 (2022) 120496.
[33] A. Ghosh, S.F.T. Kallungal, S. Ramaprabhu, 2D metal-organic frameworks: properties, synthesis, and applications in electrochemical and optical biosensors, Biosensors 13 (2023) 123.
[34] Y. Xiao, C. Chen, Y. Wu, Y. Yin, H. Wu, H. Li, Y. Fan, J. Wu, S. Li, X. Huang, W. Zhang, B. Zheng, F. Huo, Fabrication of two-dimensional metal-organic framework nanosheets through crystal dissolution-growth kinetics, ACS Appl. Mater. Interfaces 14 (2022) 7192–7199.
[35] Y. Wang, L. Li, L. Yan, X. Gu, P. Dai, D. Liu, J.G. Bell, G. Zhao, X. Zhao, K. M. Thomas, Bottom-up fabrication of ultrathin 2D Zr metal-organic framework nanosheets through a facile continuous microdroplet flow reaction, Chem. Mater. 30 (2018) 3048–3059.
[36] W. Wu, X. Cai, X. Yang, Y. Wei, L. Ding, L. Li, H. Wang, Accurate stacking engineering of MOF nanosheets as membranes for precise H_2 sieving, Nat. Commun. 15 (2024) 10730.
[37] C. Crivello, S. Sevim, O. Graniel, C. Franco, S. Pané, J. Puigmartí-Luis, D. Muñoz-Rojas, Advanced technologies for the fabrication of MOF thin films, Mater. Horiz. 8 (2021) 168–178.
[38] X. Wang, M. Wang, M. Chen, Y. Zhang, A mini review of ceramic-based MOF membranes for water treatment, Membranes 13 (2023) 751.
[39] Q. Xing, X. Xu, H. Li, Z. Cui, B. Chu, N. Xie, Z. Wang, P. Bai, X. Guo, J. Lyu, Fabrication methods of continuous pure metal-organic framework membranes and films: a review, Molecules 29 (2024) 3885.
[40] M. Miyamoto, S. Kohmura, H. Iwatsuka, Y. Oumi, S. Uemiya, In situ solvothermal growth of highly oriented Zr-based metal organic framework UiO-66 film with monocrystalline layer, CrystEngComm 17 (2015) 3422–3425.
[41] Y. Cheng, S.J. Datta, S. Zhou, J. Jia, O. Shekhah, M. Eddaoudi, Advances in metal-organic framework-based membranes, Chem. Soc. Rev. 51 (2022) 8300–8350.
[42] X. Guo, F. Zhang, D.G. Evans, X. Duan, Preparation of layered double hydroxide films with different orientations on the opposite sides of a glass substrate by in situ hydrothermal crystallization, Chem. Commun. (2009) 6836–6838.
[43] L. Ye, X. Chen, Y. Gao, X. Ding, J. Hou, S. Cao, Ultrathin two-dimensional metal-organic framework nanosheets for efficient electrochemical CO_2 reduction, J. Energy Chem. 57 (2021) 627–631.